Plasmonics (2021) 16:37–48
https://doi.org/10.1007/s11468-020-01262-z

Surface-Plasmon-Induced Ag Nanoparticles Decorated In_2O_3 Nanowires for Low Noise Photodetectors

Amitabha Nath[1] · Mitra Barun Sarkar[1]

Received: 21 July 2020 / Accepted: 11 August 2020 / Published online: 14 August 2020

Abstract

Silver (Ag) nanoparticles (NPs) were synthesized by glancing angle deposition (GLAD) technique on indium oxide (In_2O_3) nanowires (NWs) over n-type Si substrate. The In_2O_3 NWs and Ag NPs were morphologically characterized by field emission scanning electron microscopy (FESEM) and electron dispersive spectroscopy (EDS). The complete growth of In_2O_3 NWs was observed by high-resolution transmission electron microscopy (HRTEM) and corresponding selected area electron diffraction (SAED) pattern was also studied. The structural analysis was done by high-resolution X-ray diffraction (HRXRD), and relevant peaks were identified to calculate the crystalline size. The HRXRD patterns displayed the peak for Ag NPs and monoclinic crystal structure of Ag_3O_4. The optical properties were analyzed by photoluminescence (PL) emission spectrums. The presence of Ag NPs over In_2O_3 NWs reduced the PL intensity. Atomic force microscopy (AFM) was also studied to estimate the surface roughness for both the samples. The semi-logarithmic *I-V* (*ln*(*I*)-*V*) characteristics revealed the enhancement in photoconduction for the n-Si/In_2O_3 NWs/Ag NPs device at − 4.5 V using a 100-W tungsten filament source. The total ~ 2.6 fold enhancement in photosensitivity were recorded for the n-Si/In_2O_3 NWs/Ag NPs device at an applied voltage of − 2.4 V. This n-Si/In_2O_3 NWs/Ag NPs device possessed high detectivity and low noise equivalent power (NEP) as compared with the bare n-Si/In_2O_3 NWs device.

Keywords GLAD · In_2O_3 nanowires · Ag nanoparticles · Surface plasmon · Photodetector

Introduction

In the field of optoelectronics technology, indium oxide (In_2O_3) is a most frequently used direct bandgap (~ 3.6 eV) semiconductor material [1, 2]. Many nanocrystalline oxides materials like TiO_2, ZnO In_2O_3 etc. are broadly used because of their remarkable physical and chemical properties [3–6]. Among all the metal oxides, In_2O_3 shows flawless advantages in optoelectronics applications like solar cells [7], sensors [8], photodetectors [9], organic light-emitting diodes (OLEDs) [10] etc., due to very good electrical transparency, synthesis method, large-area uniformity and mechanical flexibility. There are numerous physical techniques that have been introduced to fabricate the In_2O_3 nanostructures like sputtering [11], laser ablation [12], electron beam evaporation [13] and thermal evaporation [14], which make it too costly to be commercially produced. Earlier, It was reported that the plasmonic metal NPs like Cu [15], Au [16] and Ag [17] reduces the reflection of incident photons and it exhibits robust surface plasmon resonance (SPR) behaviour. Nevertheless, to controlling SPR, the behaviour size, shape and separation between two NPs assume a noteworthy role. Glancing angle deposition or GLAD is an attractive option for fabricating In_2O_3 photodetectors because, in addition to being a reliable, sophisticated technique with in situ characterization and control, it is a cheap, one-step process. It has been already reported that Au/TiO_2 nanorod arrays having imminent applications in the efficient solar energy conversion [18]. NWs and NPs are very appealing for photodetectors for their high surface-to-volume ratio compared with their sizes and high controllability in growth with advanced techniques [19, 20]. In this research paper, the authors were fabricated In_2O_3 NWs (~ 400 nm) and Ag NPs (~ 10 nm) based In_2O_3 NWs over n-type silicon (Si) substrate using a double step glancing angle deposition (GLAD) cum electron beam (e-beam) evaporation technique. It has been shown that the plasmonic Ag NPs-based device is superior compared with the In_2O_3 NW device in terms of photoconduction. Therefore, simply employing structural phenomenon, the optical properties of metal NPs can be

✉ Mitra Barun Sarkar
mbarun.ece@nita.ac.in

[1] Microelectronics and Nanoelectronics Laboratory, Department of Electronics and Communication Engineering, National Institute of Technology Agartala, Jirania 799046, India

transformed [21]. Gorurla et al. reported that Au-ZnO plasmonic device has greater photoresponsitivity than Ag-GaN-based device [22]. Li et al. also reported that plasmonic enhancement by metal NPs deals with novel opportunities to progress the performance of optoelectronic devices [23]. So, the fabrication of metal NPs is relatively a very challenging task. Fabrication of metal NPs was reported by J. Fu et al. using GLAD technique [24]. Mehta et al. reported In_2O_3:Ag nanocomposite layers by chemical capping and dip-coating method for the application of gas sensing properties [25]. Zhou et al. also reported that the GLAD technique was an incredible and active technique for monitoring the morphology, thickness and shape of the nanostructured samples [26]. So, Ag NPs oriented In_2O_3 NWs device is one of the effective and unique structure to develop photodetector in the optoelectronics applications, and to the best of our knowledge, no such reports have been published regarding the combined NPs-NWs structure using GLAD-assisted e-beam evaporation technique, thus making it more attractive with commercial off-the-shelf devices.

In this research paper, an easy and inimitable fabrication technique has been illustrated to synthesize Ag NPs coated In_2O_3 NWs by GLAD technique. This technique was controlled inside the e-beam evaporator system. The growth of In_2O_3 NWs and Ag NPs was observed and relevant information was extracted through FESEM and HRTEM analysis. Manifestation of Ag NPs and formation of Ag_3O_4 compound was identified by HRXRD investigation. Further, the PL intensity was studied and subsequent degradation in PL intensity was observed. The surface roughness was calculated using AFM analysis. With all morphological and structural characteristics, the photoconduction properties were analysed through In contact, and relevant results were studied. The improvement in photoconduction was observed for the In_2O_3 NWs/Ag NPs device and the improved detectivity, low noise equivalent power response was also recorded.

Experimental

In_2O_3 NWs (~400 nm) (Highly pure 99.999%, MTI Corporation, USA) and Ag NPs (~10 nm) were deposited over the pre-cleaned Si wafer (Highly pure 99.999%, n-type, <100>, 4″ dia × 0.525 mm, bulk resistivity: 10 Ω cm, sheet resistance: 190 Omega/sq.) using a double-step GLAD technique by e-beam (Hind High Vacuum Co. (p) Ltd., 15F6) evaporator. The n-Si substrates were cleaned with tetrachloroethylene (C_2C_{l4}), methanol (CH_3OH) and DI water (H_2O). The solution of hydrofluoric acid (HF) + DI water (H_2O) was used at a volume ratio of 1:50 to etch native oxide from the n-Si substrate. The vacuum chamber pressure of ~2×10^{-5} mbar and the deposition rate of 1.2 $ÅS^{-1}$ are maintained during entire experimental work. The highly pure In_2O_3 and Ag pellets were placed perpendicularly ~25 cm from the substrate in the vacuum chamber with an azimuthal angle of 85° and GLAD rotation of ~130 and ~460 rpm was maintained for both the depositions, respectively. In_2O_3 and Ag pellets were evaporated between the melting current of ~10 mA to 40 mA. Here, Fig. 1 shows the full GLAD setup for the fabrication of In_2O_3 NWs and Ag NPs inside the e-beam evaporator. Total five successful depositions were carried out to deposit the ~400 nm of vertical In_2O_3 NWs. Indium (In) (Highly pure 99.999%, MTI Corporation, USA) contact has been fabricated on the GLAD: In_2O_3 NWs and In_2O_3 NWs/Ag NPs sample at a melting current less than 30 mA through the metal mask hole. The area of deposited In contact was ~1.96×10^{-7} m^2 and thickness of the contacts was ~33 nm. The two devices thus fabricated are n-Si/In_2O_3 NW/In and n-Si/In_2O_3 NW/Ag NP/In.

The samples were morphologically characterized by field emission scanning electron microscopy (FESEM, Carl-ZEISS) and energy dispersive spectroscopy (EDS, Carl-ZEISS). The growth of NWs was characterized by high-resolution transmission electron microscopy (HRTEM, JEM-2100) and corresponding selected area electron diffraction (SAED) was done on the sample. The atomic force microscopy (AFM, Bruker Multimode 8) and high-resolution X-ray diffraction (HRXRD, Bruker D8 Advanced, Cu-Kα radiation, 1.542 Å) were done to study the structural characterization. The room temperature (T = 300 K) PL study was done on the samples using Hitachi F-7000 Fluorescence Spectrophotometer with an excitation wavelength of 350 nm to study the optical characteristics. The photoconduction analysis was done using a Keysight B2902A source and

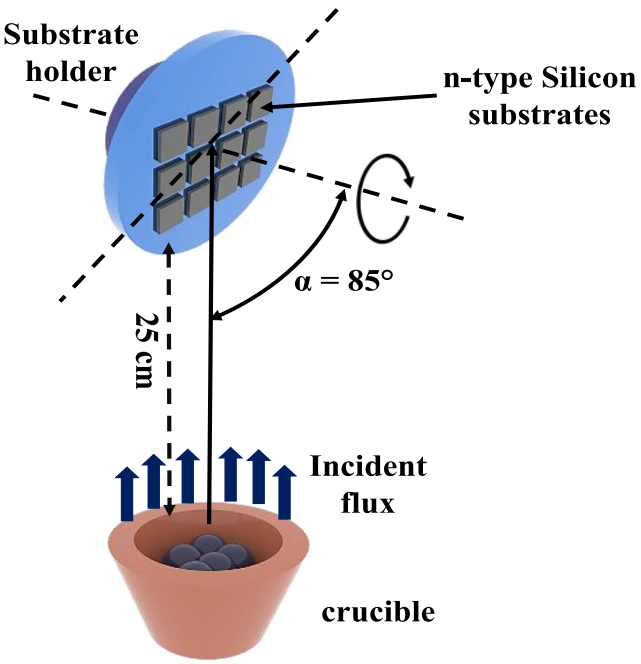

Fig. 1 Experimental setup of GLAD for the fabrication of In_2O_3 NWs and Ag NPs inside the e-beam evaporator

measurement unit (SMU) on the devices using a 100-W tungsten filament source.

Results and Discussions

FESEM and EDS Analysis

The FESEM images were displayed to study the morphological and structural characteristics of the fabricated samples. Figure 2(a), (b) and inset Fig. 2(b) show the 55° tilted view of In_2O_3 NWs, top view of Ag NPs and side view of Ag NPs decorated In_2O_3 NWs. The careful observation of FESEM images confirms the Ag NPs were densely filled and evenly distributed all over the surface. Likewise, the 55° tilted view also reveals the much attired and uneven formation of In_2O_3 NWs over the n-type substrate. The individual NWs and Ag NPs are interconnected to each other due to the high substrate temperature [20]. The average diameter of the fabricated single In_2O_3 NW was calculated around ~ 24 nm from the Fig. 2(a). In GLAD technique, the Ag NPs were fabricated due to self-atomic shadowing effect on the arbitrarily deposited seeds. Though, this type of physical evaporation technique is a very classy technique, due to GLAD rotation speed (~ 130

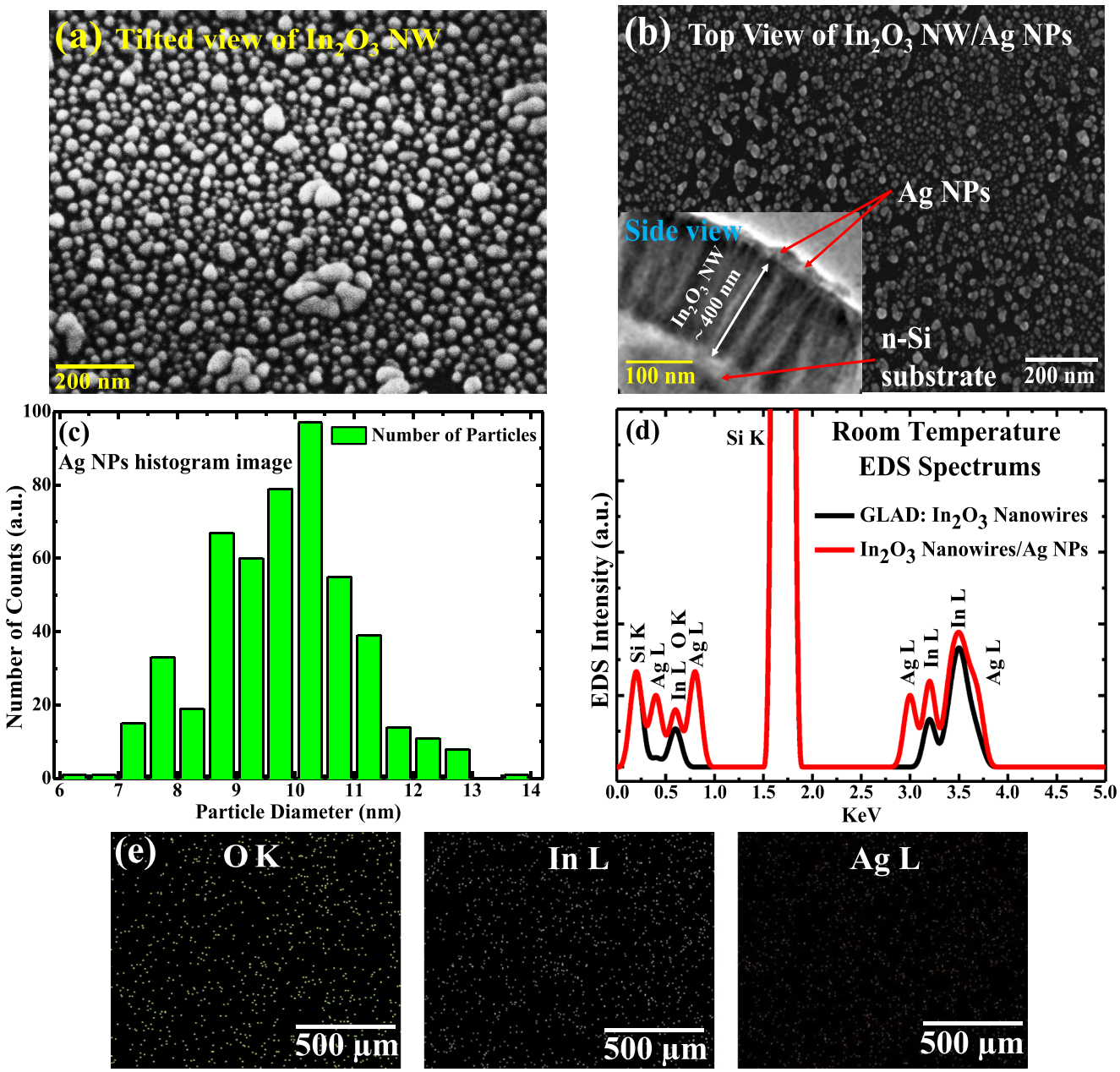

Fig. 2 (**a**) Tilted view FESEM images of In_2O_3 NWs, (**b**) Top view of the FESEM images of Ag NPs (inset side view of Ag NPs decorated In_2O_3 NWs), (**c**) Ag NPs size histogram image, (**d**) EDS analysis and (**e**) Colour mapping

and ~ 460 rpm for In_2O_3 NWs and Ag NPs), deposition angle, evaporation rate, substrate temperature etc. [13, 27].

According to Fick's law, diffusion coefficient (D_{coff}) can be found from the equation; $D_{coff} \alpha\ exp\ (-\ E_d/K_bT_s)$, where, E_d is called diffusion energy, K_b is Boltzmann constant and T_s is the temperature of the substrate. The substrate temperature (room temperature) effects in a large diffusion coefficient, which may be the reason for the formation of In_2O_3 NWs over the substrate [20]. R. Lahiri et al. reported that the formation of different length In_2O_3 NWs due to inherent atomic shadowing property by GLAD technique [28]. A low deposition rate of 1.2 $ÅS^{-1}$ and substrate temperature (room temperature) were maintained for the deposition of Ag NPs, thus formed the connected Ag NPs throughout the sample surface due to the large diffusion coefficient of Ag molecules [20]. Figure 2(c) indicated the particle size histogram image, which is extracted from Fig. 2(b). This histogram image shows that the Ag NPs consists of different NPs size ranging from ~ 6 to ~ 14 nm. The maximum number of particles diameter was measured between the sizes of ~ 10 to ~11 nm. Q. Zhou et al. and G. Wang et al. reported that the high substrate temperature (room temperature) indicated thick and connected nanostructures likewise low substrate temperature (approximately − 40 °C) indicated thin and separated nanostructures [29, 30].

To inspect the presence of deposited materials, room temperature EDS analysis was performed. Figure 1(d) established the EDS spectra for GLAD: In_2O_3 NWs and In_2O_3 NWs/Ag NPs. The elements like silicon (Si), indium (In), silver (Ag) and oxygen (O) molecules are present on the samples. Apart from In, Ag and O, no other extra peak for any other element has been found. EDS spectrum also shows the emission from In L, Ag L and O K shells with the colour mapping of EDS images of the samples depicted in Fig. 2(e), where oxygen (O) shows the green colour, indium (In) shows the blue colour and silver (Ag) shows the orange colour. Moreover, there was a high peak emission from K shell to Si substrate.

HRTEM and HRXRD Analysis

To observe the growth of vertical NWs and examine the microstructural morphologies of the same HRTEM (JEM-2100), analysis has been done. A pull-out portion of single NW was depicted in Fig. 3(a), which shows the classic growth In_2O_3 NWs having an average top diameter of ~ 25 nm and bottom diameter of ~ 16 nm. The dusky part of the single NW was due to the existence of silicon, and the dazzling part indicates the presence of oxygen molecules. Figure 3(b) displays the selected area electron diffraction (SAED) pattern which did not contain any fringe spacing and that revealed the amorphous nature of the NW [31]. The '*d*' spacing of the crystal plane was found from the SAED pattern, and it was obtained as 2 Å, 1.1 Å and 0.8 Å (JCPDS 653170).

To investigate the structural characteristics, HRXRD profile was obtained using Bruker D8 Advanced using Cu-Kα radiation source, the wavelength of 1.54 Å in the 2θ range of 30 to 75° for GLAD: In_2O_3 NWs and In_2O_3 NWs/Ag NPs, displayed in Fig. 3(c). The bare GLAD: In_2O_3 NWs shows the amorphous nature of the sample, which was also revealed in HRTEM analysis. The HRXRD diffraction peaks for GLAD: In_2O_3 NWs were emerging at $2\theta = 38.26°$, 44.47° and 64.85° with the corresponding plane of (400), (422) and (444), respectively. All the peaks were matching with the JCPDS data (JCPDS card no. 06–0416) [32]. The In_2O_3 NWs/Ag NPs shows same diffraction peak with a new diffraction peak at $2\theta = 38.06°$ due to the presence of Ag NPs which corresponds (111) plane (JCPDS card no. 04–0783) [33, 34]. Overall 50% magnified graph of Fig. 3(c) shows a clear image of a diffraction peak at $2\theta = 38.06°$ displayed in Fig. 3(d). Likewise, its revealed another diffraction peak at $2\theta = 50.68°$ corresponds to (031) plane (JCPDS card no. 84–1261) for the monoclinic crystal structure of Ag_3O_4 [35]. The formation of the Ag–O compound shows (031) diffraction plane which indicated the monoclinic crystal structure, which was formed due to oxygen attached with the Ag NPs by attracting the oxygen molecules [36]. The average crystalline size was calculated ~ 38 and ~ 87 nm for the bare GLAD: In_2O_3 NWs and In_2O_3 NWs/Ag NPs, respectively, using Debye Scherrer equation, which was shown in equation 1.

$$D = (0.9\lambda)/(\beta^{*}\cos\theta) \tag{1}$$

where D is crystalline size, λ is the wavelength of the incident X-ray (K_α), β is the full-width half maximum (FWHM) in radians of Gaussian distribution of the HRXRD data and 2θ is the Bragg's angle measured in radians. The authors have reported the method of extraction of crystalline size [37]. The average crystalline size was increased for In_2O_3 NWs/Ag NPs due to the difference in atomic radius of Ag (144 pm) and In (167 pm). The tendency for agglomeration of Ag NPs during the process in the high ambient temperature of the chamber was maybe the reason for the increase in dimension. Lattice strain was also calculated ~ 0.0073 and ~ 0.0221 for both the same samples displayed in Fig. 3(e) (inset of Fig. 3(d)) using Williamson-Hall (*W-H*) plot equation, which was shown in equation 2.

$$\beta^{*}\cos\theta/\lambda = k/\mathrm{D} + 4\varepsilon\sin\theta/\lambda \tag{2}$$

where k is the shape factor, ε is lattice strain and 2θ is the Bragg's diffraction angle. Correspondingly in that case, the lattice strain was increased, and it offers the work hardening process in the material [38].

PL Emission

Room temperature PL emission has been done between the wavelengths of 350 and 650 nm using an excitation

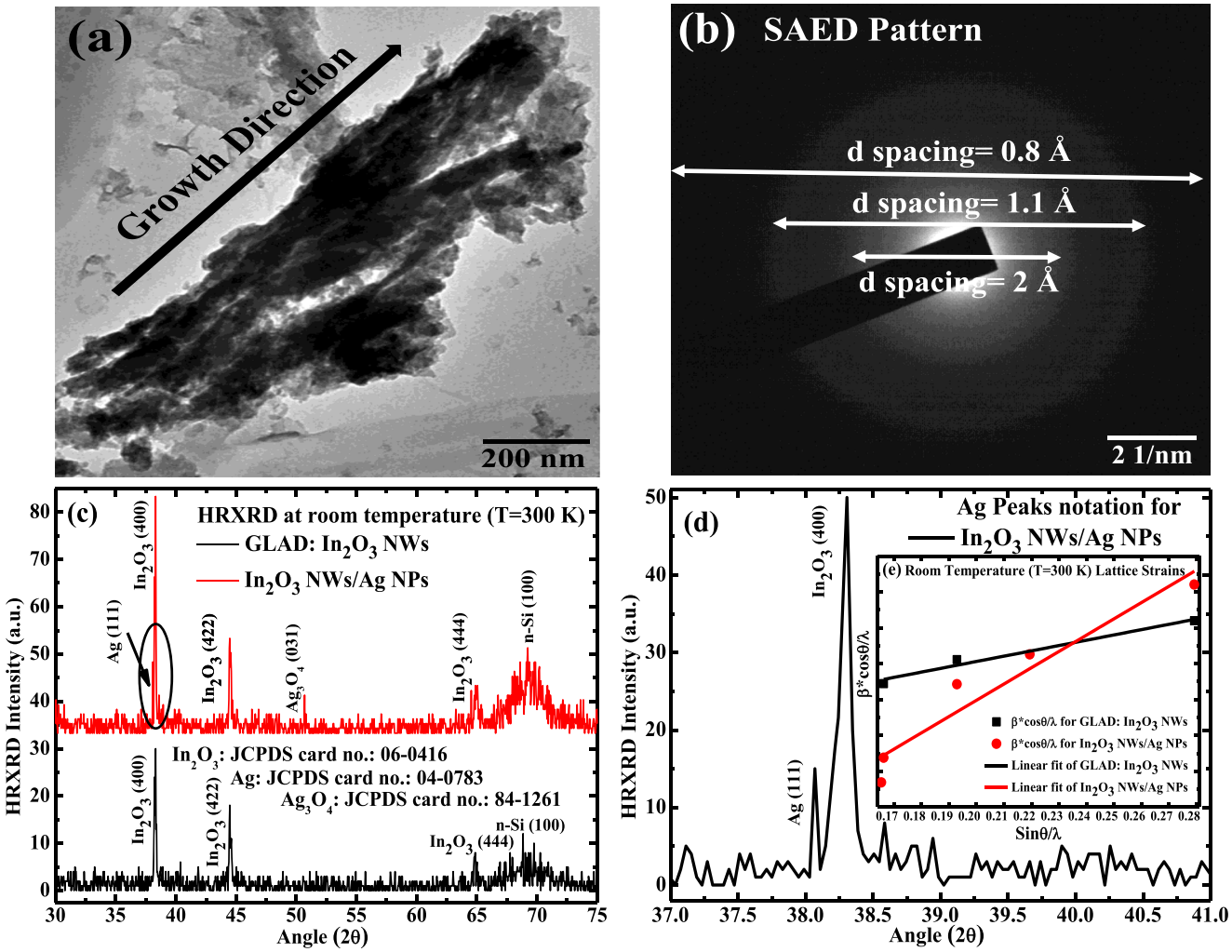

Fig. 3 (**a**) HRTEM analysis of In_2O_3 NWs, (b) SAED pattern of In_2O_3 NWs, (**c**) HRXRD spectrums of GLAD: In_2O_3 NWs and In_2O_3 NWs/Ag NPs (**d**) 50% magnified spectrums of In_2O_3 NWs/Ag NPs and (e) Lattice strain of GLAD: In_2O_3 NWs and In_2O_3 NWs/Ag NPs (inset of Fig. 3(d))

wavelength of 350 nm by Hitachi F-7000 Fluorescence Spectrophotometer with a Xenon light source of 150 watt for the bare GLAD: In_2O_3 NWs and In_2O_3 NWs/Ag NPs samples presented in Fig. 4.

The GLAD: In_2O_3 NWs and In_2O_3 NWs/Ag NPs indicated the PL emission spectrums at 440 nm (~2.81 eV) and 466 nm (~2.66 eV) with the full-width half maximum (FWHM) of ~ 71 nm and ~48 nm, respectively. In_2O_3 shows the PL emission spectrum between 400 and 500 nm due to the existence of oxygen vacancies in the material [39]. The blue region emission arises at 440 nm for the GLAD: In_2O_3 NWs attributed new energy levels in the forbidden energy gap. This type of emission occurred due to the recombination of electron-hole pairs at the surface of the samples. Zheng et al. reported that the PL emissions of 429 and 460 nm occurred for the In_2O_3 NWs samples [40]. It was apparent that the high PL intensity manifested a higher rate of recombination of electro-hole pairs and the low PL intensity indicates a lower rate of recombination of electro-hole pairs. Additionally, The Ag NPs created a

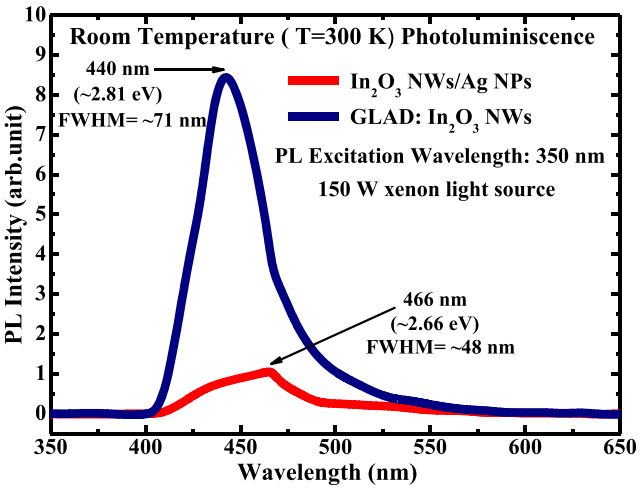

Fig. 4 PL emission spectrum for GLAD: In_2O_3 NWs and In_2O_3 NWs/Ag NPs using an excitation wavelength of 350 nm

precise bond with the GLAD: In_2O_3 NWs and formed an inorganic silver compound particle like Ag_3O_4. This type of inorganic silver compound was observed in the room temperature ($T = 300$ K) through HRXRD analysis. These Ag_3O_4 particles act as trap particles to capture the photo-induced electrons in the forbidden energy gap and thus defeat the recombination of electron and holes [41]. In the experiment, a decrease in ~ 8.5-fold PL intensity was observed for the In_2O_3 NWs/Ag NPs sample due to the aforementioned reason. Here, with the reduction in PL intensity, a ~ 26-nm red shift had been observed for the In_2O_3 NWs/Ag NPs samples as compared with that of the bare GLAD: In_2O_3 NWs samples due to the SPR effect. Kim et al. reported a similar type of emission due to oxygen-related defect states [39]. Fong et al. also reported that the Ag NPs attached with In_2O_3 NWs and produced SPR effect, which shifted the resonance peak to longer wavelength [42]. Conclusively, the presence of Ag NPs over In_2O_3 NWs shifted the resonance peak and enhanced the emission at ~ 466 nm. Therefore, the PL emission analysis delivered the SPR effect using the Ag NPs over the In_2O_3 NWs.

AFM Analysis

Figure 5(a) and 5(b) shows the three dimensional (3D) AFM images for the bare GLAD: In_2O_3 NWs (height: ~ 400 nm) and In_2O_3 NWs/Ag NPs samples. The overall scan area of 10 μm × 10 μm and resolution of 2 μm were maintained for both the samples. The Ag NPs were milled up with In_2O_3 NWs and created Ag NPs–In_2O_3 layer because of the electrostatic charge-charge interaction between metal-semiconductor junctions [43]. The root mean square surface roughness (R_p) was calculated ~ 6.10 nm for the GLAD: In_2O_3 NWs sample and ~ 5 nm for In_2O_3 NWs/Ag NPs sample, which will be reduced by ~ 1.22-fold. The packing density of In_2O_3 nanostructures was predisposed by the newly formed Ag NPs over In_2O_3 NWs that leads to the reduction in surface roughness. Antonio Ruiz Puigdollers and others also reported that the same theory on the formation of Ag and Au clusters over the different materials [44].

Photoconduction Analysis

To study the electrical behaviour of bare GLAD: In_2O_3 NWs and In_2O_3 NWs/Ag NPs samples, indium (In) metallization was performed in the e-beam chamber. Figure 6(a) and 6(b) shows the 3-D layout design of the bare n-Si/In_2O_3 NWs/In (device-1) and n-Si/In_2O_3 NWs/Ag NPs/In (device-2) devices. Figure 6(c) displays the room temperature semi-logarithmic *I-V* (*ln*(*I*)-*V*) characteristics for both the devices using B2902A source and measurement unit (SMU) and a 100-W tungsten filament source. In this case, almost no changes in dark current conduction and trifling changes in light current conduction had been observed under the forward bias condition. Likewise, under reverse bias mode, a low dark current conduction was observed for device-2, moreover light current for device-2 (~ 4 mA) was higher than device-1 (~ 3.2 mA). The enhancement in light current may be due to trapping of electrons at the interface of the In_2O_3 NWs/Ag NPs followed by trapping and de-trapping process of electrons [45, 46]. Trapping of electrons at the interface was started under dark current measurement likewise de-trapping of electrons was started under light current measurement. The enhancement of current attributed to the abovementioned de-trapping process and due to oxygen-related trap states, it reduces the depletion region in the structures and allows the tunnelling of electrons [47]. Lee et al. also reported a similar type of observation in their research work [45]. The ideality factor (η) was calculated ~ 20 and ~ 11 for device-1 and device-2, respectively, from the slope and intercept of semi-logarithmic forward bias of *I-V* characteristics, represented

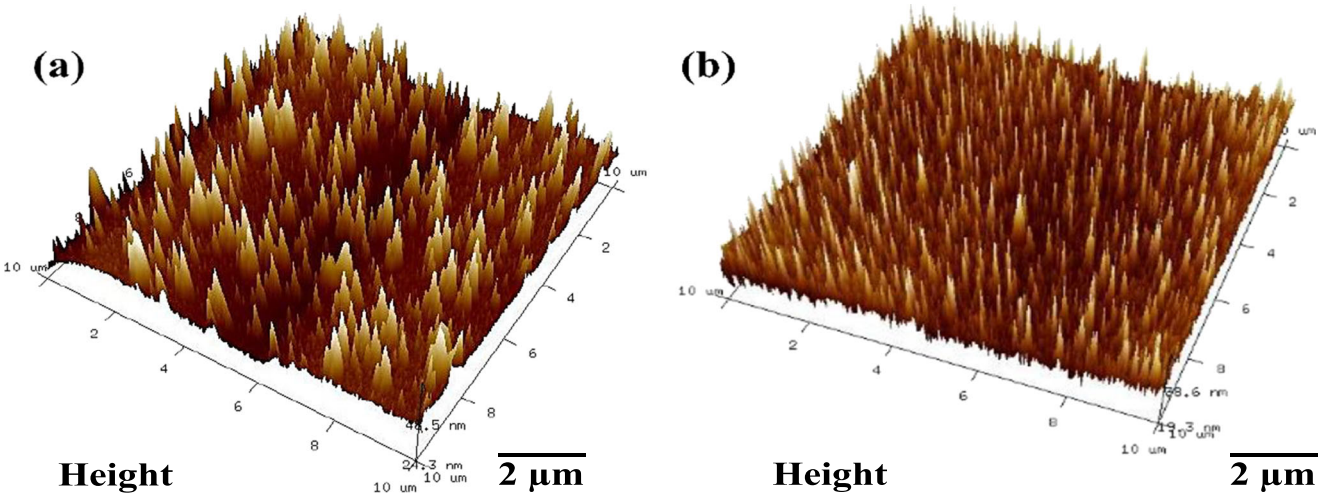

Fig. 5 AFM images of (**a**) GLAD: In_2O_3 NWs and (**b**) In_2O_3 NWs/Ag NPs

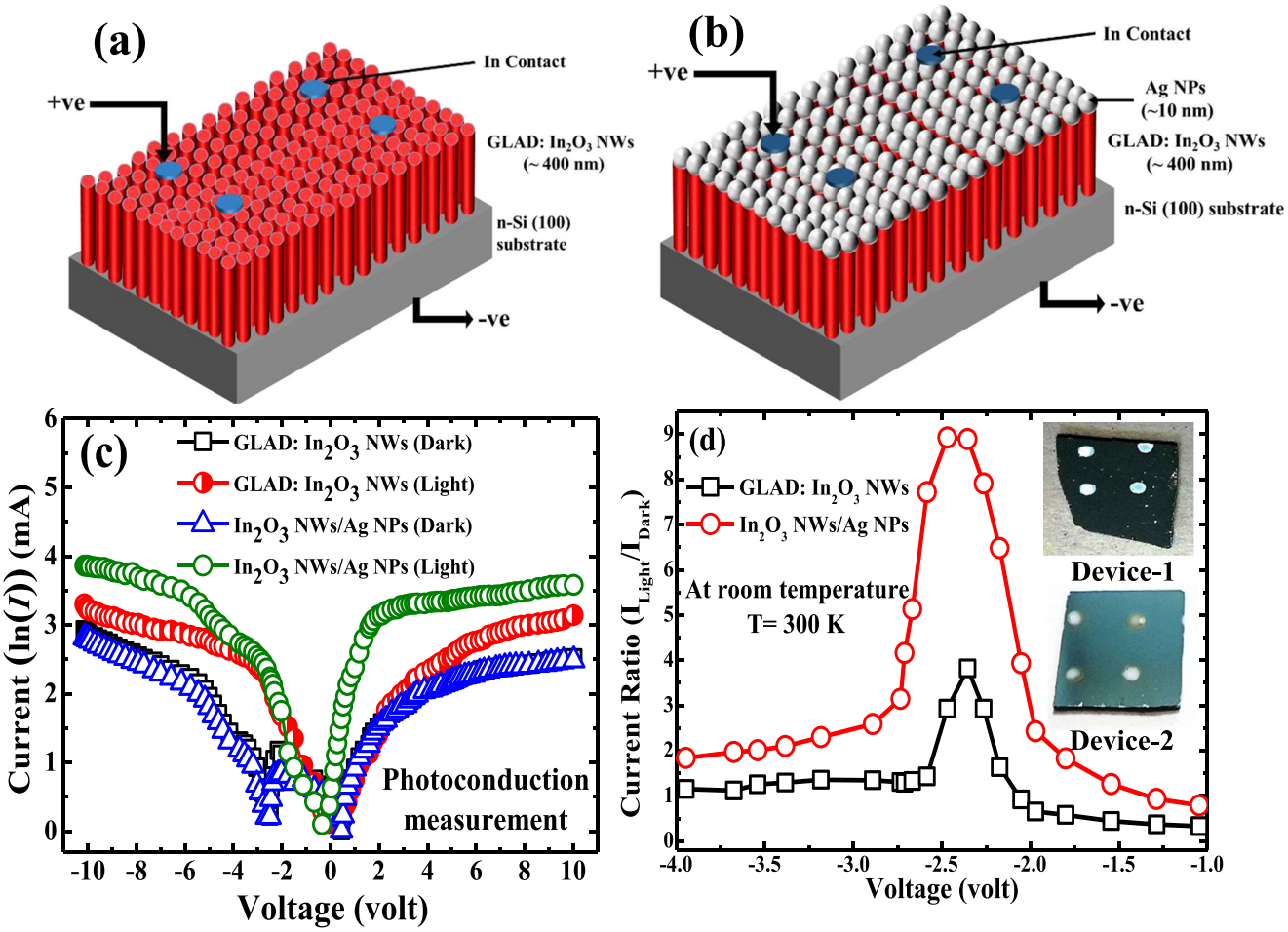

Fig. 6 3-D Layout design of (**a**) GLAD: In_2O_3 NWs device (device-1), (**b**) In_2O_3 NWs/Ag NPs (device-2), (**c**) Semi-logarithmic current (*I*)-voltage (*V*) characteristics for GLAD: In_2O_3 NWs and In_2O_3 NWs/Ag NPs, (**d**) Current ratio (I_{light}/I_{dark})-voltage graph for both the devices

in Fig. 5(c). The method of extraction of the ideality factor for a diode was reported by Devi et al. using equation-3,

$$\eta = \frac{q}{kT}\frac{1}{\frac{\partial(\ln(I))}{\partial V}} \tag{3}$$

where k is called Boltzmann constant, T is absolute temperature, q is an electron charge and $\frac{\partial(\ln(I))}{\partial V}$ is the slope of the semi-logarithmic *I-V* curve [48, 49].

The photosensitivity (I_{light}/I_{dark}) for both the devices was calculated in reverse bias mode from the applied voltage of − 1 to − 4 V, displayed in Fig. 6(d). At − 2.4 V applied bias, ~ 2.6-fold enhancement was observed for the device-2 as compared with that of the device-1. This enhancement in photosensitivity was due to the SPR effect and a sufficient number of dangling bonds at the surface of In_2O_3 NWs/Ag NPs device, which can easily attract the oxygen molecules and hence the maximum electron tunnelling happened [47]. The SPR effect and dangling bonds enhanced the oxygen molecules over the surface of device-2, and thus, photosensitivity was increased. A clear colour change from deep blue to light blue confirms the formation of Ag NPs on the device-2 (Fig. 6(d), inset).

The barrier height was calculated of ~ 0.6 eV and ~ 0.5 eV for bare GLAD: In_2O_3 NWs device and In_2O_3 NW/Ag NPs device, respectively, at zero bias voltage using the following equation.

$$J_0 = A^* T^2 exp\left[\frac{-q\varnothing_B}{kT}\right] \tag{4}$$

where J_0 is the reverse saturation current corresponding to zero bias, A^* is the Richardson constant, k is the Boltzmann constant, $\varnothing_B$ is the zero-bias barrier height. The decrease in barrier height was attributed to the reduction in the depletion region and tunnelling of charge carriers through the device [50]. The rectification ratio (R_{ratio}) of the two devices was calculated to investigate the device performance, depicted in inset Fig. 7. The R_{ratio} was defined as $\frac{|I_F|}{|I_R|}$, where I_F and I_R is forward and reverse dark current. At ~ 3 V, the R_{ratio} was found to be maximum (approximately twofold) in case of

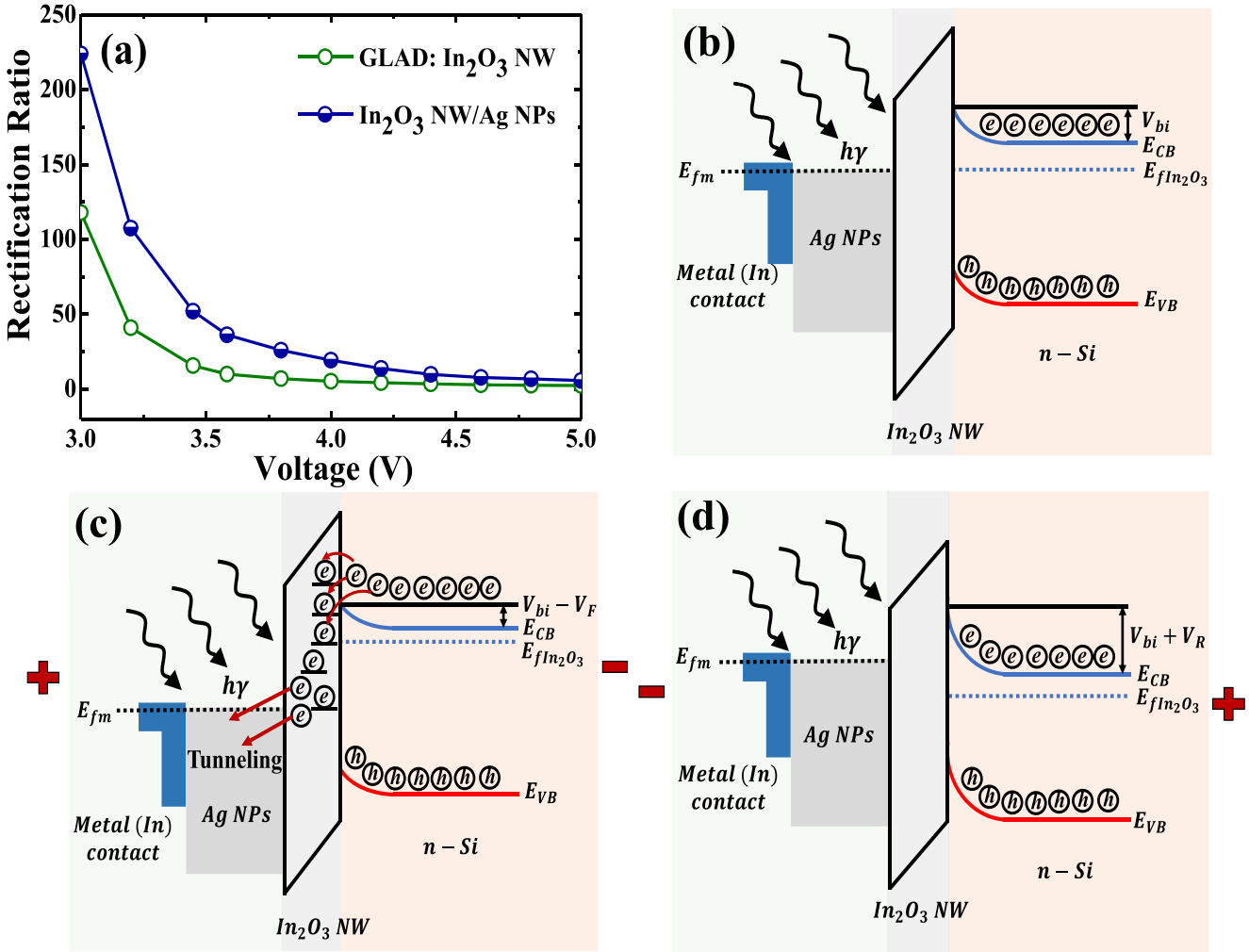

Fig. 7 (**a**) Rectification ratio for GLAD: In_2O_3 NWs and In_2O_3 NWs/Ag NPs devices. In_2O_3 NWs/Ag NPs device band diagram for (**b**) zero bias, (**c**) forward bias and (**d**) reverse bias under light illumination

In_2O_3 NW/Ag NPs device compared with the bare In_2O_3 NW device, which shows better rectification capability. A high R_{ratio} exhibited good rectifying behaviour in dark illumination and attributed high electron mobility in the In_2O_3 NW/Ag NPs device [51]. Figure 7(b-d) shows the band diagram for zero bias, forward bias and reverse bias under light illumination condition, respectively.

In case of forward bias, the n-Si and In_2O_3 NW junction was connected to negative voltage whereas In and Ag NPs junction was connected to positive voltage. Under light illumination, the charge carriers can be highly separated by n-Si and In_2O_3 NW junction, and there was a flow of photogenerated electrons through Ag NPs/In_2O_3 NW junction which can be collected through In and Ag NPs junction. Furthermore, when the positive voltage was applied at In contact, In and Ag/In_2O_3 interface states can trap the electrons at the conduction band (E_{CB}), as seen in Fig. 7(c). This reduces the width of the depletion region, barrier height and hence trap-assisted tunnelling of photogenerated electrons happened, which enhanced the photosensitivity [19]. Moreover, Ag has higher electronegative value (electronegativity: 1.93) thus attracts the oxygen molecules in Ag NPs/In_2O_3 NW device. The attraction of oxygen by Ag from In_2O_3 induces oxygen-assisted defect states in the Ag NPs/In_2O_3 NW device [52]. In case of reverse bias (Fig. 7(d)), the n-Si and In_2O_3 NW junction was connected to positive voltage whereas In and Ag NPs junction was connected to a negative voltage. As a result under light illumination, the photocurrent was enhanced, which may be due to the separation of photoexcited carriers by Ag NPs/In_2O_3 NW junction as well as it leads to increase in the width of depletion region, and therefore, no tunnelling has occurred [19].

The authors were also plotted specific detectivity (D^*) and noise equivalent power (NEP) from $ln(I)$-V characteristics using the below equations to determine the detectors properties, displayed in Fig. 8(a) and 8(b), respectively.

$$D^* = \frac{R}{\sqrt{2e\,J_{dark}}} \tag{5}$$

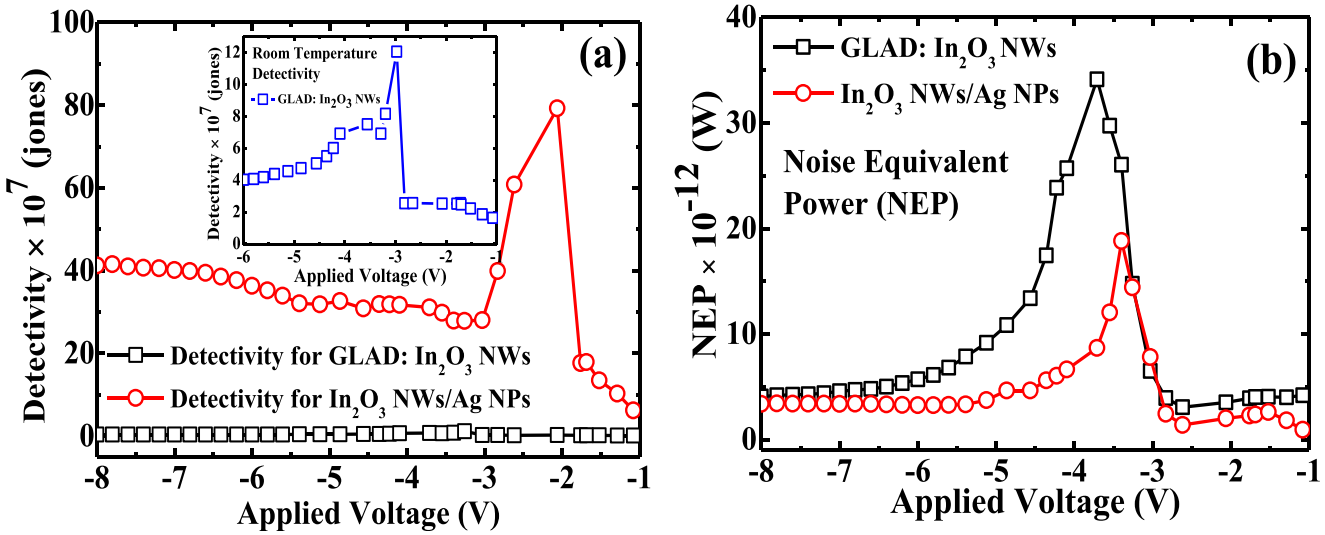

Fig. 8 (**a**) Detectivity vs. voltage graph for the GLAD: In_2O_3 NWs and In_2O_3 NWs/Ag NPs device. (**b**) Detectivity vs. voltage graph for the GLAD: In_2O_3 NWs (inset of Fig. 7(a)). (**c**) NEP vs. voltage graph for both the same devices

$$\mathrm{NEP} = \frac{\sqrt{A}}{D^*} \tag{6}$$

where R is the responsivity of the devices, e is the charge of an electron and J_{dark} is current density under dark illumination, A is the particular device area [20]. The maximum detectivity of $\sim 78 \times 10^7$ jones (Fig. 8(a)) for the device − 2 was observed from the applied voltage of − 8 to − 1 V, which possesses ~ 6.5-fold boost-up as compared with that of device-1 (Fig. 8(a), inset). The augmentation in detectivity was achieved due to the low dark current and SPR effect in the device-2. Wang et al. reported the enhancement in detectivity was due to low dark current levels in the Ag NPs surrounded ZnO thin film photodetector [53]. The low NEP was observed $\sim 19 \times 10^{-12}$ W (Fig. 8(b)) for the device-2 at the same applied voltage, and it retains the ~ 1.8-fold low NEP as compared with that of device-1. In our case, the calculated NEP was lower than the previously reported values [54, 55]. The comparison of different outcomes of this work with other reported works based on their performance was depicted in Table 1. Additionally, the traps reduces the occurrence of generation-recombination, which may decrease the NEP and enhances D^*. Moreover, the low NEP results in the high detectivity and increased in photocurrent for the Ag NPs based device, which provides a flexible opportunity to use In_2O_3 NWs/Ag NPs device as a low noise photodetector for optoelectronics applications.

Conclusion

In this paper, the authors successfully synthesized Ag NPs over In_2O_3 NWs using a double-step GLAD technique. From HRTEM image, the average diameter of ~ 25 nm and bottom diameter of ~ 16 nm of single NW have been extracted. The '*d*' spacing of 2 Å, 1.1 Å and 0.8 Å was calculated from SAED pattern, and it displays the amorphous nature of the In_2O_3 NWs. HRXRD profile exhibits the formation of monoclinic Ag_3O_4 compound over the In_2O_3 NWs, which indicated the Ag–O compound with (031) diffraction plane. The PL emission of In_2O_3 NWs/Ag NPs displayed the red shifting of spectrum at 466 nm (~ 2.66 eV) due to the scattering of SPR effect by Ag_3O_4 compound over the In_2O_3 NWs. The mitigation of ~ 1.22-fold root mean square surface

Table 1 Comparison of different outcomes of this work with other reported works based on their performance

Device structure	Device type	Detectivity (jones)	NEP (watt)	References
n-Si/In_2O_3 NW/Ag NPs	Metal-oxide-semiconductor detector	78×10^7 = (7.8×10^8)	19×10^{-12}	this device
Al_2O_3/AlGaN/Si	MIS detector	4.52×10^8	48×10^{-12}	[54]
GaN /Ni	Schottky barrier	1.57×10^7	9.95×10^{-8}	[55]
AlGaN/GaN	MSM detector	2.85×10^7	1.62×10^{-8}	[56]
Al/SiO_2/GaN	MIS detector	2.03×10^8	2.19×10^{-9}	[57]

roughness was observed for the In_2O_3 NWs/Ag NPs, which affects the packing density in the In_2O_3 nanostructures. The n-Si/In_2O_3 NWs device and n-Si/In_2O_3 NWs/Ag NPs devices were created using In top contact through metallization process. At − 4.5 V, the n-Si/In_2O_3 NWs/Ag NPs/In device shows higher light current due to the coupling of SPR effect of Ag NPs as compared with the n-Si/In_2O_3 NWs/In device under a 100-W tungsten filament source. The enhancement in light current attributed de-trapping process due to the oxygen-related trap states which reduces the depletion region in the structures and allows the tunnelling of electrons. The ideality factor of ~ 20 and ~ 11 was calculated for the n-Si/In_2O_3 NWs/In device and n-Si/In_2O_3 NWs/Ag NPs/In devices. The maximum ~ 2.6-fold enhancement in photosensitivity was observed at an applied bias of − 2.4 V due to the SPR effect in the n-Si/In_2O_3 NWs/Ag NPs/In device. The maximum specific detectivity of $\sim 78 \times 10^7$ jones and low NEP of $\sim 19 \times 10^{-12}$ W were observed for the devices from the applied voltage of − 8 to − 1 V, which possess ~ 6.5-fold enhancement in detectivity and ~ 1.8-fold low NEP in the Ag NPs decorated device. Therefore, the whole technical experimental process signifies that it can be used as an efficient Ag NP-based plasmonic photodetector for optoelectronics applications with better photosensitivity in the existing technology.

Acknowledgements The authors are acknowledged to SAIF, NEHU Shillong for HRTEM analysis. The authors are thankful to Centre of Excellence (COE) in Advanced Materials, NIT Durgapur and Central Instrumentation Centre (CIC), Tripura University, INDIA for providing the cross-section and top FESEM facility respectively. The authors are also thankful to Dr. S. P. Mondal and Dr. B. Saha, Assistant Professors, Department of Physics, NIT Agartala, INDIA for providing the AFM and HRXRD facility, respectively.

References

1. Woo JK, Cho S (2014) Electrical and optical properties of Eu-doped indium oxide thin films deposited by radio-frequency magnetron sputtering. J Nanosci Nanotechnol 14(12):8982–8986. https://doi.org/10.1166/jnn.2014.10081
2. Jothibas M, Manoharan C, Jeyakumar SJ, Praveen P (2015) Study on structural and optical behaviors of In_2O_3 nanocrystals as potential candidate for optoelectronic devices. J Mater Sci Mater Electron 26(12):9600–9606. https://doi.org/10.1007/s10854-015-3623-x
3. Sarkar MB, Choudhuri B, Bhattacharya P, Barman RN, Ghosh A, Dwivedi SMMD, Chakrabartty S, Mondal A (2018) Improved UV photodetection by indium doped TiO_2 thin film based photodetector. J Nanosci Nanotechnol 18(7):4898–4903. https://doi.org/10.1166/jnn.2018.15295
4. Sarkar MB, Mondal A, Choudhuri B (2016) Presence of capacitive memory in indium doped TiO_2 alloy thin film. J Alloys Compd 654:529–533. https://doi.org/10.1016/j.jallcom.2015.09.129
5. Hu Y, Chen HJ (2007) Preparation and characterization of nanocrystalline ZnO particles from a hydrothermal process. J Nanopart Res 10(3):401–407. https://doi.org/10.1007/s11051-007-9264-0
6. Seetha M, Bharathi S, Raj AD, Mangalaraj D, Nataraj D (2009) Optical investigations on indium oxide nano-particles prepared through precipitation method. Mater Charact 60(12):1578–1582. https://doi.org/10.1016/j.matchar.2009.09.009
7. Charalampous A, Zervos M, Kioseoglou J, Tsagaraki K, Androulidaki M, Konstantinidis G, Tanasă E, Vasile E (2019) Epitaxially oriented Sn:In_2O_3 nanowires grown by the vapor-liquid-solid mechanism on m-, r-, a-Al_2O_3 as scaffolds for nanostructured solar cells. ACS Appl Energy Mater 2(6):4274–4283. https://doi.org/10.1021/acsaem.9b00519
8. Lee SK, Chang D, Yang SD, Kim SW (2015) Synthesis of Diacid-assisted indium oxide nanoparticles and its CO gas sensing activity. J Nanosci Nanotechnol 15(12):9905–9910. https://doi.org/10.1166/jnn.2015.10867
9. Shao D, Qin L, Sawyer S (2012) Near ultraviolet photodetector fabricated from polyvinyl-alcohol coated In_2O_3 nanoparticles. Appl Surf Sci 261:123–127. https://doi.org/10.1016/j.apsusc.2012.07.111
10. Hong JS, Kim SM, Park SJ, Choi HW, Kim KH (2010) Preparation of In_2O_3-ZnO (IZO) thin film on glass substrate for organic light emitting device (OLED). Mol Cryst Liq Cryst 520(1):19/[295]–27/[303]. https://doi.org/10.1080/15421401003608287
11. Hashimoto R, Abe Y, Nakada T (2008) High mobility titanium-doped In_2O_3 thin films prepared by sputtering/post-annealing technique. Appl Phys Express 1(1):015002. https://doi.org/10.1143/APEX.1.015002
12. Zhang D, Liu Z, Li C, Tang T, Liu X, Han S, Lei B, Zhou C (2004) Detection of NO_2 down to ppb levels using individual and multiple In_2O_3 nanowire devices. Nano Lett 4(10):1919–1924. https://doi.org/10.1021/nl0489283
13. Han SD, Noh MS, Kim S, Shim YS, Song YG, Lee K, Lee HR, Nahm S, Yoon SJ, Kim JS, Kang CY (2017) Versatile approaches to tune a nanocolumnar structure for optimized electrical properties of In_2O_3 based gas sensor. Sens Actuators B Chem 248:894–901. https://doi.org/10.1016/j.snb.2017.01.108
14. Peng XS, Wang YW, Zhang J, Wang XF, Zhao LX, Meng GW, Zhang LD (2002) Large-scale synthesis of In_2O_3 nanowires. Appl Phys A Mater Sci Process 74(3):437–439. https://doi.org/10.1007/s003390101037
15. Zhang JZ, Noguez C (2008) Plasmonic optical properties and applications of metal nanostructures. Plasmonics. 3(4):127–150. https://doi.org/10.1007/s11468-008-9066-y
16. Sobhani A, Lauchner A, Najmaei S, Ayala-Orozco C, Wen F, Lou J, Halas NJ (2014) Enhancing the photocurrent and photoluminescence of single crystal monolayer MoS_2 with resonant plasmonic nanoshells. Appl Phys Lett 104(3):031112. https://doi.org/10.1063/1.4862745
17. Xiao XH, Ren F, Zhou XD, Peng TC, Wu W, Peng XN, Yu XF, Jiang CZ (2010) Surface plasmon-enhanced light emission using silver nanoparticles embedded in ZnO. Appl Phys Lett 97(7):071909. https://doi.org/10.1063/1.3480417
18. Arshad MS, Trafela Š, Rožman KŽ, Kovač J, Djinović P, Pintar A (2017) Determination of Schottky barrier height and enhanced photoelectron generation in novel plasmonic immobilized multisegmented (Au/TiO_2) nanorod arrays (NRAs) suitable for solar energy conversion applications. J Mater Chem C 5(40):10509–10516. https://doi.org/10.1039/c7tc02633a
19. Pooja P, Chinnamuthu P (2020) Surface state controlled superior photodetection properties of Isotype n-TiO2/In2O3 heterostructure nanowire array with high specific detectivity. IEEE Trans Nanotechnol 19:34–41. https://doi.org/10.1109/tnano.2019.2956960
20. Ghosh A, Dwivedi SMMD, Ghadi H, Chinnamuthu P, Chakrabarti S, Mondal A (2017) Boosted UV sensitivity of Er-doped In_2O_3 thin films using plasmonic Ag nanoparticle-based surface texturing. Plasmonics. 13(3):1105–1113. https://doi.org/10.1007/s11468-017-0679-x

21. Marimuthu A, Zhang J, Linic S (2013) Tuning selectivity in propylene epoxidation by plasmon mediated photo-switching of cu oxidation state. Science 339(6127):1590–1593. https://doi.org/10.1126/science.1231631
22. Gogurla N, Sinha AK, Santra S, Manna S, Ray SK (2014) Multifunctional au-ZnO Plasmonic nanostructures for enhanced UV photodetector and room temperature NO sensing devices. Sci Rep 4(1):6483. https://doi.org/10.1038/srep06483
23. Li D, Sun X, Song H, Li Z, Chen Y, Jiang H, Miao G (2012) Realization of a high-performance GaN UV detector by nanoplasmonic enhancement. Adv Mater 24(6):845–849. https://doi.org/10.1002/adma.201102585
24. Fu J, Zhao Y (2010) Au nanoparticle based localized surface plasmon resonance substrates fabricated by dynamic shadowing growth. Nanotechnology 21(17):175303. https://doi.org/10.1088/0957-4484/21/17/175303
25. Mehta BR, Singh VN (2005) Structural, electrical and gas-sensing properties of In_2O_3:Ag composite nanoparticle layers. Pramana J Phys 65(5):949–958. https://doi.org/10.1007/BF02704096
26. Zhou CM, Gall D (2007) Growth competition during glancing angle deposition of nanorod honeycomb arrays. Appl Phys Lett 90(9):093103. https://doi.org/10.1063/1.2709929
27. Robbie K, Brett MJ (1997) Sculptured thin films and glancing angle deposition: growth mechanics and applications. J Vac Sci Technol A 15(3):1460–1465. https://doi.org/10.1116/1.580562
28. Lahiri R, Mondal A (2018) Superior memory of Er doped TiO_2 nanowire MOS capacitor. IEEE Electron Device Lett 39:1856–1859. https://doi.org/10.1109/LED.2018.2874272
29. Zhou Q, Li Z, Ni J, Zhang Z (2011) A simple model to describe the rule of glancing angle deposition. Mater Trans 52(3):469–473. https://doi.org/10.2320/matertrans.M2010342
30. Wang G, Liu Y, Gao C, Guo L, Chi M, Ijiro K, Maeda M, Yin Y (2017) Island growth in the seed-mediated overgrowth of monometallic colloidal nanostructures. Chem. 3(4):678–690. https://doi.org/10.1016/j.chempr.2017.08.004
31. Ann Mary KA, Unnikrishnan NV, Philip R (2015) Cubic to amorphous transformation of Se in silica with improved ultrafast optical nonlinearity. RSC Adv 5(18):14034–14041. https://doi.org/10.1039/C4RA14025G
32. Anand K, Kaur J, Singh RC, Thangaraj R (2016) Structural, optical and gas sensing properties of pure and Mn-doped In_2O_3 nanoparticles. Ceram Int 42(9):10957–10966. https://doi.org/10.1016/j.ceramint.2016.03.233
33. Koohpeima F, Mokhtari MJ, Khalafi S (2017) The effect of silver nanoparticles on composite shear bond strength to dentin with different adhesion protocols. J Appl Oral Sci 25(4):367–373. https://doi.org/10.1590/1678-7757-2016-0391
34. Shameli K, Ahmad MB, Zamanian A, Sangpour P, Shabanzadeh P, Abdollahi Y, Zargar M (2012) Green biosynthesis of silver nanoparticles using Curcuma longa tuber powder. Int J Nanomedicine 7:5603–5610. https://doi.org/10.2147/IJN.S36786
35. Laskri A, Drici A, Boulouma A, Amara A, Bernede JC (2019) Investigation of microstructural and optical properties of Ag_3O_4 thin films sprayed onto glass substrate. JNanoR. 58:90–101. https://doi.org/10.4028/www.scientific.net/JNanoR.58.90
36. Xie W, Li Y, Sun W, Huang J, Xie H, Zhao X (2010) Surface modification of ZnO with Ag improves its photocatalytic efficiency and photostability. J Photochem Photobiol A Chem 216(2–3):149–155. https://doi.org/10.1016/j.jphotochem.2010.06.032
37. Nath A, Raman R, Yadav VK, Sannibabu P, Sarkar MB (2020) Bandgap modulation of glancing angle deposition aided Ag nanoparticles covered TiO_2 thin film by high temperature annealing. J Nanosci Nanotechnol 20(12):7636–7643. https://doi.org/10.1166/jnn.2020.18575
38. Chiou ST, Tsai HL, Lee WS (2007) Effects of strain rate and temperature on the deformation and fracture behaviour of titanium alloy. Mater Trans 48(9):2525–2533. https://doi.org/10.2320/matertrans.MRA2007607
39. Kim WJ, Pradhan D, Sohn Y (2013) Fundamental nature and CO oxidation activities of indium oxide nanostructures: 1D-wires, 2D-plates, and 3D-cubes and donuts. J Mater Chem A 1(35):10193–10202. https://doi.org/10.1039/c3ta12312j
40. Zheng MJ, Zhang LD, Li GH, Zhang XY, Wang XF (2001) Ordered indium-oxide nanowire arrays and their photoluminescence properties. Appl Phys Lett 79(6):839–841. https://doi.org/10.1063/1.1389071
41. Jeong S, Garnett EC, Wang S, Yu Z, Fan S, Brongersma ML, McGehee MD, Cui Y (2012) Hybrid silicon Nanocone-polymer solar cells. Nano Lett 12(6):2971–2976. https://doi.org/10.1021/nl300713x
42. Fong KE, Yung LYL (2013) Localized surface plasmon resonance: a unique property of plasmonic nanoparticles for nucleic acid detection. Nanoscale. 5(24):12043–12071. https://doi.org/10.1039/c3nr02257a
43. Yang D, Jang J, Lim J, Lee JK, Kim SH, Hong JI (2016) Correlations of optical absorption, charge trapping, and surface roughness of TiO_2 photoanode layer loaded with neat Ag-NPs for efficient perovskite solar cells. ACS Appl Mater Inter 8(33):21522–21530. https://doi.org/10.1021/acsami.6b07079
44. Puigdollers AR, Schlexer P, Pacchioni G (2015) Gold and silver clusters on TiO_2 and ZrO_2 (101) surfaces: role of dispersion forces. The J Phys Chem C 119(27):15381–15389. https://doi.org/10.1021/acs.jpcc.5b04026
45. Lee CJ, Won CH, Lee JH, Hahm SH, Park H (2019) GaN-based ultraviolet passive pixel sensor on silicon (111) substrate. Sensors. 19(5):1051. https://doi.org/10.3390/s19051051
46. Shamir N, Mihaychuk JG, van Driel HM (2000) Trapping and detrapping of electrons photoinjected from silicon to ultrathin SiO_2 overlayers. I In vacuum and in the presence of ambient oxygen. J Appl Phys 88(2):896–908. https://doi.org/10.1063/1.373753
47. Sarkar MB, Mondal A, Choudhuri B, Mahajan BK, Chakrabartty S, Ngangbam C (2014) Enlarged broad band photodetection using indium doped TiO_2 alloy thin film. J Alloys Compd 615:440–445. https://doi.org/10.1016/j.jallcom.2014.06.184
48. Devi VL, Jyothi I, Reddy VR, Choi CJ (2012) Schottky barrier parameters and interfacial reactions of rapidly annealed au/cu bilayer metal scheme on N-type InP. Open Appl Physics J 5(1):1–9. https://doi.org/10.2174/1874183501205010001
49. Mohanraj K, Balasubramanian D, Chandrasekaran J, Bose AC (2018) Synthesis and characterizations of Ag-doped CdO nanoparticles for P-N junction diode application. Mater Sci Semicond Process 79:74–91. https://doi.org/10.1016/j.mssp.2018.02.006
50. Zheng H, Mahajan BK, Su SC, Mukherjee S, Gangopadhyay K, Gangopadhyay S (2016) Barrier modification of metal-contact on silicon by Sub-2 nm platinum nanoparticles and thin dielectrics. Sci Rep 6(1):25234. https://doi.org/10.1038/srep25234
51. Yuan Z (2014) A photodiode with high rectification ratio and low turn-on voltage based on ZnO nanoparticles and SubPc planar heterojunction. Phys E 56:160–164. https://doi.org/10.1016/j.physe.2013.09.001
52. Nath S, Kar JP, Myoung JM (2011) Junction properties and applications of ZnO single nanowire based Schottky diode, Nanowires-Fundamental Research. InTech, Rijeka, pp 161–182
53. Wang H, Lim JW, Mota FM, Jang YJ, Yoon M, Kim H, Hu W, Nohc YY, Kim DH (2017) Plasmon-mediated wavelength-selective enhanced photoresponse in polymer photodetectors. J Mater Chem C 5(2):399–407. https://doi.org/10.1039/C6TC04662B
54. Liu HY, Hsu WC, Chou BY, Wang YH (2015) Fabrication AlGaN/GaN MIS UV Photodetector by H_2O_2 oxidation. IEEE Photon Technol Lett 27(1):101–104. https://doi.org/10.1109/lpt.2014.2362911

55. Chen TP, Young SJ, Chang SJ, Huang BR, Wang SM, Hsiao CH, Wu SL, Yang CB (2012) Low-frequency noise characteristics of GaN Schottky barrier photodetectors prepared with nickel annealing. IEEE Sensors J 12(9):2824–2829. https://doi.org/10.1109/jsen.2012.2200886
56. Lee KH, Chang PC, Chang SJ, Wang YC, Yu CL, Wu SL (2009) Characterization of AlGaN/GaN metal- semiconductor-metal photodetectors with a low-temperature AlGaN interlayer. IEEE Sensors J 9(6):723–727. https://doi.org/10.1109/jsen.2009.2021190
57. Chiou YZ, Su YK, Chang SJ, Gong J, Chang CS, Liu SH (2003) The properties of photo chemical-vapor deposition SiO_2 and its application in GaN metal-insulator semiconductor ultraviolet photodetectors. J Electron Mater 32(5):395–399. https://doi.org/10.1007/s11664-003-0164-5